

A computational study of the mechanical behavior of nanocrystalline fcc metals

Yujie Wei, Cheng Su, Lallit Anand *

Department of Mechanical Engineering, Massachusetts Institute of Technology, Room 1-310C, 77 Massachusetts Avenue, Cambridge, MA 02139, USA

Received 7 February 2006; received in revised form 24 February 2006; accepted 2 March 2006

Available online 5 June 2006

Abstract

We have conducted a finite-element-based study of the deformation and failure behavior of nanocrystalline face-centered cubic metals. A rate-dependent amorphous plasticity model which accounts for cavitation and related failure phenomena is used to model the grain boundaries, while a crystal plasticity model is used for the grain-interiors. Our numerical simulations using material parameters estimated to represent the macroscopic rate-dependent stress–strain response of nanocrystalline nickel (nc-Ni), show that there is a transition in deformation mechanism from grain-interior shearing to grain-boundary shearing, as the average grain-size decreases from 50 nm to 10 nm, and that the low ductility of nc-Ni is the result of intergranular failure due to grain-boundary shearing and resulting cavitation at triple-junctions and other high stress points in the microstructure. Our numerical simulations also show that the strength of nc-Ni is expected to be slightly higher in compression than in tension, primarily due to the easier operation of cavitation failure of the grain boundaries in tension.

© 2006 Acta Materialia Inc. Published by Elsevier Ltd. All rights reserved.

Keywords: Nanocrystalline metals; Continuum modeling; Finite-element method

1. Introduction

Nanocrystalline metals are polycrystalline metallic materials with grain sizes typically less than 100 nm. These materials have been the subject of intense, worldwide research over the past two decades, and due to this research activity the micromechanisms governing their macroscopic mechanical behavior are now beginning to be better understood (e.g. [1,2]). Recent reviews on the topic, and references to the vast amount of literature, may be found in Kumar et al. [3] and Wolf et al. [4]. Nanocrystalline metals contain a high volume fraction of “grain-boundary”-intercrystalline regions. For example, idealizing a unit cell containing a crystalline grain interior and an intercrystalline grain-boundary region as a sphere of diameter d , with

an intercrystalline shell of thickness δ and a crystalline core of diameter $d - 2\delta$, the volume fractions of grain-boundary regions for a fixed value of $\delta \sim 0.5$ nm, and grain sizes d of 10 nm and 40 nm are 27.1% and 7.3%, respectively. Thus, a substantial fraction of the atoms in nanocrystalline materials lie in the intercrystalline grain-boundary regions, and these regions play an increasingly significant role as the grain size decreases below the 100 nm level. The nature of the intercrystalline grain-boundary regions depends on how the material has been processed. High-resolution transmission electron microscopy (TEM) studies on nanocrystalline materials show that while many grain boundaries appear sharp and well-defined, others show considerable disorder, with the maximum disordered region (measured perpendicular to grain boundaries) being approximately 2–3 lattice spacings; i.e., less than 1 nm [5].

In this paper we focus our attention on continuum-level modeling of the low temperature mechanical response of nanocrystalline fcc metals. A broad picture of the operative

* Corresponding author. Tel.: +1 617 253 1635; fax: +1 617 258 8742.
E-mail address: anand@mit.edu (L. Anand).

micromechanisms of inelastic deformation in this class of materials in this temperature range is beginning to emerge. The following features of the operative micromechanisms are now reasonably widely-accepted [1–4,6–8]:

- There is a strong interplay between dislocation-based deformation in the crystalline grain interiors and the inelastic deformation mechanisms operative in the grain-boundary regions.
- Grain boundaries act as both sources and sinks for dislocations.
- Let Γ denote the stacking fault energy of the face-centered cubic (fcc) material, G its nominal shear modulus, and b the magnitude of the Burgers vector of a perfect dislocation, then there exists a critical grain size d_c , given by $d_c \approx (2/3)(Gb^2/\Gamma)$, above which plastic deformation in nanocrystalline grain interiors occurs by the emission of complete dislocations from grain boundaries, and below which the plastic deformation occurs by emission of partial dislocations. The partial dislocations produce stacking faults as they glide through the grains [9,10].
- The number of dislocations or stacking faults that need to traverse a typical grain in the nanocrystalline range to produce an overall strain of the order of 5% is quite small, typically less than 10–15. Thus, dislocation based plasticity in the grain interiors is quite discrete in nature.
- When the grain size d becomes smaller than d_c , dislocation-based slip processes become less effective in producing overall inelastic deformation, and grain-boundary-region-based inelastic deformation mechanisms start to dominate [11–13].
- The grain-boundary inelastic deformation mechanisms are loosely called “grain-boundary sliding”, but at low temperatures atomistic simulations show this to be stress-activated shear-shuffling of atoms located in the intercrystalline regions, and the cooperative result of numerous such shear-shuffles leads to substantial overall shearing of the intercrystalline regions; this process is not dominated by thermal diffusion of atoms in the grain-boundary regions. Such a deformation mechanism is reminiscent of that in metallic glasses, where inelastic deformation occurs by local shearing of clusters of atoms – “shear transformation zones” [14].
- Nanocrystalline fcc materials show a room-temperature strain-rate sensitivity which is almost an order of magnitude higher than their microcrystalline counterparts. The mechanism underlying this enhanced strain-rate sensitivity is not fully understood at present, but is probably due to the enhanced strain rate sensitivity of the intercrystalline grain-boundary regions, relative to the rate sensitivity of the crystalline grain-interiors.
- The ductility of these materials, as measured by elongation in tensile experiments, is significantly reduced from the values observed for their microcrystalline counterparts, and seldom exceeds 5%. Since this occurs even for materials at the high end of grain sizes in the nanocrystalline range (~ 100 nm), one can infer that even

though there is some accommodation of the overall imposed deformation by dislocation-mediated plasticity in the grain interiors, this accommodation is insufficient. Additional, intergranular accommodation mechanisms, such as cavitation and microcracking, must be operative. It must be noted that while widespread distributed grain-boundary damage prior to final macroscopic fracture has not been experimentally observed, atomistic simulations do show void formation and decohesion leading to intergranular fracture in nanocrystalline materials [6–8].

As reviewed in [3,4], much of the understanding of the micromechanisms operative during the inelastic deformation of nanocrystalline materials has been obtained from large-scale molecular dynamics (MD) studies published in the past few years. Although MD methods of studying atomic-level mechanical response of materials are useful for gaining valuable insight, these methods are at present not suitable for carrying out simulations of deformation and failure under conditions similar to those under which physical experiments on nanocrystalline materials are carried out, i.e., macroscopic-sized specimens with complicated boundary conditions, involving realistic strain rates. MD simulations are inherently limited to small, idealized microstructures and extremely high strain rates, typically $>10^7/\text{s}$, which corresponds to a strain of 1% in 1 ns.

In contrast to MD methods, finite-element methods (FEM) for simulation of micromechanical interactions and prediction of local as well as overall response of materials have been effectively used to study the mechanical response of variety of composite material systems in recent years, and such methods do not possess the major limitations of the MD methods listed above. However, use of continuum-mechanical-based FEM methods is contingent upon the assumptions of continuum mechanics – suitable smoothness of displacement fields, the notion of stress, and balance laws of linear and angular momentum – continuing to hold at the nanoscale. Further, just as the results from MD simulations depend crucially on the reliability of the interatomic potentials used in such studies, the results of FEM simulations depend crucially on the reliability of the continuum-level constitutive equations used in such analyses. While the concepts of continuum elasticity are expected to be approximately applicable at small scales approaching the nano-level, the concepts of classical continuum plasticity being applicable at this scale are highly questionable. Nevertheless, based on a pragmatic engineering approach, and bolstered by the success of (length-scale-independent) crystal-plasticity theories and attendant FEM simulation methodologies to represent grain-scale shear localization phenomena and texture evolution (cf., e.g. [15]), a few investigators have recently carried out continuum-level FEM simulations of the inelastic deformation and failure response of nanocrystalline materials (cf., e.g. [17,18]). Although

in their infancy, such FEM-based simulations also provide valuable insights on the deformation and failure response of nanocrystalline materials; insights which cannot solely be obtained from atomistic simulations or physical experiments.

For example, Wei and Anand [17] coupled a single-crystal plasticity constitutive model for the grain interior, with a cohesive interface constitutive model to account for grain-boundary sliding and separation phenomena. They recognized that a standard crystal plasticity model for the grain-interior deformation, which implicitly assumes enough dislocation nucleation and multiplication to result in a sufficiently smooth macroscopic response, is inadequate to represent the limited amount of inelastic deformation due to emission and eventual absorption of the relatively fewer (partial or complete) dislocations from grain boundaries in nanocrystalline materials. However, since elastic anisotropy and crystallographic texture effects are still important in nanocrystalline materials, and since the few dislocations in these materials are still expected to move on slip systems, the mathematical structure of a continuum crystal plasticity theory is still useful as an indicator of the limited inelasticity due to crystalline slip within the nanocrystalline grains. Their cohesive interface model for grain boundaries accounts for both reversible elastic, as well as irreversible inelastic sliding-separation deformations at the grain boundaries prior to failure. The tensile and shear properties of the cohesive grain boundaries were estimated by fitting results of numerical simulations to experimentally-measured stress–strain curves for nanocrystalline electrodeposited Ni. Unfortunately, such a fitting procedure makes it difficult to unambiguously characterize the grain-boundary properties, and they used a value for the shear strength of the grain boundaries which was very similar in magnitude to the tensile strength of the boundaries; as is clear from the recent atomistic simulations of grain-boundary response in Sansoz and Molinari [7], this assumption is clearly unrealistic. Also, Wei and Anand [17] restricted their models for the grain interiors and grain boundaries to be completely rate-independent.

Warner et al. [18], following the methodology of Wei and Anand [17], have also used a continuum FEM method to model the plastic deformation of nanocrystalline copper by using crystal plasticity for the grain interiors and cohesive elements for grain boundaries. For the traction–separation relations for the grain boundaries, they obtained estimates for the shear and normal response of the boundaries from quasi-continuum atomistic calculations. Since their atomistic calculations were carried out at 0 K, they had to use a large ad hoc thermal-correction (cf. their Eq. (8)) to estimate the shear strength for the grain boundaries in Cu at room temperature.

As is clear from our brief review, continuum-level FEM simulations of the inelastic deformation and failure response of nanocrystalline materials are still in their infancy. Much needs to be done to refine the constitutive models, specially for the traction–separation relations in

approaches using cohesive elements to represent grain boundaries.

Here, motivated by the fact that amorphous metals are the ultimate limit for nanocrystalline metals, as the crystal grain size decreases to zero, and that a new strain-rate-dependent continuum-plasticity theory for amorphous metals at low homologous temperatures is now available [19,20], we have developed a slightly modified version of the continuum theory for amorphous metals to represent the intercrystalline grain-boundary regions. We do not use interface traction–separation relations; instead we use the stress–strain relations from this continuum theory to represent the grain-boundary response. We have coupled this with a single-crystal plasticity model for the crystalline grain interiors in a “composite”-type approach to model the deformation and failure response of nanocrystalline materials.

It is the purpose of this paper to report on our constitutive models and the results from our numerical simulations. Specifically, we have (a) developed a modified version of the rate-dependent amorphous plasticity model of Anand and Su [19,20] to account for cavitation and related failure phenomena, and used such a model to represent the grain-boundary response of nanocrystalline materials; and (b) accounted for the transition from partial dislocation to complete dislocation mediated plasticity for the grain interiors. This development is based on the recent work of Zhu et al. [10].

The plan of this paper is as follows. The amorphous plasticity model we have adopted to represent the rate-dependent deformation and failure of grain boundaries is described in Section 2. In Section 3, we describe the model that we have used to represent grain interior plasticity due to partial or perfect dislocations. In Section 4 we study the response of a prototypical grain-boundary as modeled by our theory for amorphous materials. Numerical representation of two-dimensional microstructures with different grain sizes is briefly discussed in Section 5. Applications of the model to represent the deformation and failure response of Ni over a range of grain sizes in the nanocrystalline regime are reported in Section 6. We close in Section 7 with some final remarks.

2. A constitutive model for the elastic–viscoplastic deformation of grain boundaries

Our continuum-mechanical constitutive model for the intercrystalline grain-boundary regions in nanocrystalline materials is based on a modification of the theory of Anand and Su [19,20] for amorphous metallic materials, to account for cavitation failure. Using standard notation of modern continuum mechanics, the underlying constitutive equations relate the following basic fields: χ , motion; $\mathbf{F} = \nabla \chi$ with $J = \det \mathbf{F} > 0$ deformation gradient; \mathbf{F}^p with $J^p = \det \mathbf{F}^p > 0$, plastic deformation gradient; $\mathbf{F}^e = \mathbf{F}\mathbf{F}^{p-1}$ with $J^e = \det \mathbf{F}^e > 0$, elastic deformation gradient; $\mathbf{F}^e = \mathbf{R}^e \mathbf{U}^e$, polar decomposition of \mathbf{F}^e ; $\mathbf{U}^e = \sum_{\alpha=1}^3 \lambda_{\alpha}^e \mathbf{r}_{\alpha} \otimes \mathbf{r}_{\alpha}$, spectral

decomposition of \mathbf{U}^e ; $\mathbf{E}^e = \sum_{\alpha=1}^3 (\ln \lambda_{\alpha}^e) \mathbf{r}_{\alpha} \otimes \mathbf{r}_{\alpha}$, logarithmic elastic strain; \mathbf{T} with $\mathbf{T} = \mathbf{T}^T$, Cauchy stress; $\mathbf{T}^e = \mathbf{R}^{eT} (\mathbf{J}^e \mathbf{T}) \mathbf{R}^e$, stress conjugate to elastic strain \mathbf{E}^e . The set of constitutive equations is summarized below:

2.1. Equation for the stress

$$\mathbf{T}^e = 2G\mathbf{E}^e + (K - (2/3)G)(\text{tr} \mathbf{E}^e) \mathbf{1} \quad (1)$$

with G and K the elastic shear modulus and bulk modulus, respectively. \mathbf{T}^e has the spectral representation $\mathbf{T}^e = \sum_{i=1}^3 \sigma_i \hat{\mathbf{e}}_i \otimes \hat{\mathbf{e}}_i$, where $\{\sigma_i\}$ are the principal values, and $\{\hat{\mathbf{e}}_i\}$ are the orthonormal principal directions of \mathbf{T}^e . We assume that the principal stresses $\{\sigma_i\}$ are strictly ordered such that $\sigma_1 \geq \sigma_2 \geq \sigma_3$.

2.2. Evolution equation for \mathbf{F}^p

$$\dot{\mathbf{F}}^p = \mathbf{D}^p \mathbf{F}^p, \quad \mathbf{D}^p = \mathbf{D}^{pT} \quad \text{with} \quad \mathbf{D}^p = \mathbf{D}_s^p + \mathbf{D}_c^p, \quad (2)$$

where the plastic stretching \mathbf{D}^p is taken to arise from a shearing contribution \mathbf{D}_s^p controlled by the local shear stresses, and a cavitating/volumetric contribution \mathbf{D}_c^p controlled by the local tensile principal stresses and the local mean normal stress.

We assume that \mathbf{D}_s^p occurs by shearing relative to some slip systems. Slip systems are labelled by integers α ; each slip system is specified by a slip direction \mathbf{s}^α , and a slip plane normal \mathbf{m}^α with $\mathbf{s}^{(\alpha)} \cdot \mathbf{m}^{(\alpha)} = 0$, and $|\mathbf{s}^{(\alpha)}| = |\mathbf{m}^{(\alpha)}| = 1$. For an amorphous isotropic material there are no preferred directions other than the principal directions of stress, and accordingly we consider plastic flow to be possible on six potential slip systems defined relative to the principal directions of stress \mathbf{T}^e :

$$\left. \begin{aligned} \mathbf{s}^{(1)} &= \cos \vartheta \hat{\mathbf{e}}_1 + \sin \vartheta \hat{\mathbf{e}}_3, & \mathbf{m}^{(1)} &= \sin \vartheta \hat{\mathbf{e}}_1 - \cos \vartheta \hat{\mathbf{e}}_3, \\ \mathbf{s}^{(2)} &= \cos \vartheta \hat{\mathbf{e}}_1 - \sin \vartheta \hat{\mathbf{e}}_3, & \mathbf{m}^{(2)} &= \sin \vartheta \hat{\mathbf{e}}_1 + \cos \vartheta \hat{\mathbf{e}}_3, \\ \mathbf{s}^{(3)} &= \cos \vartheta \hat{\mathbf{e}}_1 + \sin \vartheta \hat{\mathbf{e}}_2, & \mathbf{m}^{(3)} &= \sin \vartheta \hat{\mathbf{e}}_1 - \cos \vartheta \hat{\mathbf{e}}_2, \\ \mathbf{s}^{(4)} &= \cos \vartheta \hat{\mathbf{e}}_1 - \sin \vartheta \hat{\mathbf{e}}_2, & \mathbf{m}^{(4)} &= \sin \vartheta \hat{\mathbf{e}}_1 + \cos \vartheta \hat{\mathbf{e}}_2, \\ \mathbf{s}^{(5)} &= \cos \vartheta \hat{\mathbf{e}}_2 + \sin \vartheta \hat{\mathbf{e}}_3, & \mathbf{m}^{(5)} &= \sin \vartheta \hat{\mathbf{e}}_2 - \cos \vartheta \hat{\mathbf{e}}_3, \\ \mathbf{s}^{(6)} &= \cos \vartheta \hat{\mathbf{e}}_2 - \sin \vartheta \hat{\mathbf{e}}_3, & \mathbf{m}^{(6)} &= \sin \vartheta \hat{\mathbf{e}}_2 + \cos \vartheta \hat{\mathbf{e}}_3, \end{aligned} \right\} \quad (3)$$

where $\vartheta = (\pi/4) + (\phi/2)$, with $\phi = \arctan \mu$ an angle of internal friction, which is defined in terms of a *friction coefficient* $\mu \geq 0$. The resolved shear and compressive normal traction on each slip system are given by

$$\tau^{(\alpha)} \stackrel{\text{def}}{=} \mathbf{s}^{(\alpha)} \cdot \mathbf{T}^e \mathbf{m}^{(\alpha)}, \quad \sigma^{(\alpha)} \stackrel{\text{def}}{=} -\mathbf{m}^{(\alpha)} \cdot \mathbf{T}^e \mathbf{m}^{(\alpha)}. \quad (4)$$

The shearing contribution \mathbf{D}_s^p is then taken to be given by

$$\mathbf{D}_s^p = \sum_{\alpha=1}^6 v^{(\alpha)} \text{sym}(\mathbf{s}^{(\alpha)} \otimes \mathbf{m}^{(\alpha)}) \quad \text{with} \quad v^{(\alpha)} = v_0 \left\{ \frac{\tau^{(\alpha)}}{c + \mu \sigma^{(\alpha)}} \right\}^{1/m} \geq 0, \quad (5)$$

where $c > 0$ is an internal variable called the cohesion. Also, v_0 is a reference plastic shear strain rate, and $m > 0$ is a strain-rate sensitivity parameter.

Next, the constitutive equation for cavitating/volumetric contribution \mathbf{D}_c^p to the plastic stretching is taken to be given by:

$$\mathbf{D}_c^p = \sum_{i=1}^3 v_c^{(i)} (\hat{\mathbf{e}}_i \otimes \hat{\mathbf{e}}_i) \quad \text{with} \quad v_c^{(i)} = \begin{cases} v_0 \left\{ \frac{\sigma_i}{\sigma_{\text{cr}}} \right\}^{1/m} & \text{if } \sigma_i > 0, \\ 0 & \text{if } \sigma_i \leq 0, \end{cases} \quad (6)$$

$$\sigma_{\text{cr}} = c_1 - c_2 \bar{\sigma}_h > 0$$

where $\bar{\sigma}_h = (1/3)(\sigma_1 + \sigma_2 + \sigma_3)$ is the mean normal stress (hydrostatic tension), and c_1 and c_2 are material parameters. In this model the contribution $v_c^{(i)} (\hat{\mathbf{e}}_i \otimes \hat{\mathbf{e}}_i)$ to \mathbf{D}_c^p is zero if the principal stress σ_i is zero or negative. When σ_i is positive, its value relative to the value of a parameter $\sigma_{\text{cr}} = \hat{\sigma}_{\text{cr}}(\bar{\sigma}_h)$, which depends on the hydrostatic tension, controls the magnitude of $v_c^{(i)}$. The value of σ_{cr} is taken to decrease linearly as the hydrostatic tension $\bar{\sigma}_h$ increases. For simplicity, the reference strain rate v_0 , and the rate sensitivity parameter m in (6) are taken to be the same as that in (5). Note that (6) predict a *spherical* inelastic cavitation only when all the principal stresses are equal to each other, $\sigma_1 = \sigma_2 = \sigma_3$. In situations where the principal stresses are unequal, the “cavitation” is predominantly in the direction of the maximum principal stress σ_1 because of the power-law nature of the relation (6).

2.3. Modeling of damage and failure of grain boundaries

We use the following simple critical-strain-based criteria to model damage and failure of grain boundaries due to cavitation. Let $\dot{\epsilon}^p = |\mathbf{D}_c^p|$ define a volumetric strain rate, and

$$\epsilon^p \stackrel{\text{def}}{=} \int_0^t \dot{\epsilon}^p(\xi) d\xi, \quad (7)$$

define a volumetric plastic strain. Then, as a simple model for damage by inelastic cavitation, we introduce a damage variable D defined by

$$D \stackrel{\text{def}}{=} \begin{cases} 0 & \text{if } \epsilon^p \leq \epsilon_{\text{cr}}^p, \\ \frac{(\epsilon^p - \epsilon_{\text{cr}}^p)}{(\epsilon_f^p - \epsilon_{\text{cr}}^p)} & \text{if } \epsilon_{\text{cr}}^p < \epsilon^p < \epsilon_f^p, \\ 1 & \text{if } \epsilon^p \geq \epsilon_f^p, \end{cases} \quad (8)$$

whose value is zero for ϵ^p less than a critical value ϵ_{cr}^p , and thereafter $D = (\epsilon^p - \epsilon_{\text{cr}}^p)/(\epsilon_f^p - \epsilon_{\text{cr}}^p)$, so that the damage variable evolves linearly towards a value of unity as ϵ^p evolves to a failure value ϵ_f^p . Correspondingly, the σ_{cr} in (6) is decreased linearly towards a value of zero $\sigma_{\text{cr}} = \{c_1 - c_2 \bar{\sigma}_h\} \times (1 - D)$. Further, to account for damage to the elastic properties, the elastic shear and bulk moduli G and K are replaced by $G \times (1 - D)$ and $K \times (1 - D)$ when damage occurs. As D approaches unity, the material is deemed to have “failed” by cavitation, and it is “removed” from the finite element calculation; in actual numerical implementation, in order to avoid numerical singularities, failure due to cavitation is deemed to

have occurred when the damage parameter D reaches a suitably large number, say ~ 0.995 . The damage model outlined above is quite rudimentary, and much work needs to be done to develop more realistic models for the transition from shear plasticity, to damage and final fracture.

3. Constitutive model for grain-interior response

We employ the standard kinematical and constitutive framework of rate-dependent single-crystal plasticity based on the multiplicative decomposition $\mathbf{F} = \mathbf{F}^e \mathbf{F}^p$ of the deformation gradient into an elastic and a plastic part (e.g. [21,22]). Here the stress $\mathbf{T}^e = (\det \mathbf{F}^e) \mathbf{F}^{e-1} \mathbf{T} \mathbf{F}^{e-\top}$ is given by $\mathbf{T}^e = \mathbb{C}[\mathbf{E}^e]$, where \mathbb{C} is the anisotropic elasticity tensor and $\mathbf{E}^e = (1/2)(\mathbf{C}^e - \mathbf{1})$ the elastic strain, with $\mathbf{C}^e = \mathbf{F}^{e\top} \mathbf{F}^e$. For cubic materials \mathbb{C} has only three independent constants, which are traditionally denoted by C_{11} , C_{12} , C_{44} .

The evolution equation for \mathbf{F}^p in this theory is

$$\dot{\mathbf{F}}^p = \mathbf{L}^p \mathbf{F}^p, \quad \mathbf{L}^p = \sum_{\alpha=1}^N v^{\alpha} \mathbf{s}_0^{\alpha} \otimes \mathbf{m}_0^{\alpha}, \quad (9)$$

where the orthonormal vector pairs $(\mathbf{m}_0^{\alpha}, \mathbf{s}_0^{\alpha})$ are crystalline slip systems, with slip direction \mathbf{s}_0^{α} and slip-plane normal \mathbf{m}_0^{α} . The microshear rates v^{α} are determined by specific constitutive functions $v^{\alpha} = \hat{v}^{\alpha}(\tau^{\alpha}, s^{\alpha})$ where $\tau^{\alpha} = \mathbf{s}_0^{\alpha} \cdot (\mathbf{C}^e \mathbf{T}^e) \mathbf{m}_0^{\alpha}$ is the resolved stress on the α th slip system, and s^{α} is a slip system deformation resistance, which for nanocrystalline materials is taken to be grain-size-dependent *constant*: i.e., no strain-hardening (cf. Eqs. (11) and (13)).

Let Γ denote the stacking fault energy of an fcc material, $G = \sqrt{(C_{11} - C_{12})C_{44}/2}$ a nominal shear modulus, and b the magnitude of the Burgers vector of a *perfect dislocation*. Then, according to a model of Asaro et al. [9,23], there exists a critical grain size d_c given by

$$d_c \approx (2/3)(Gb^2)/\Gamma, \quad (10)$$

above which plastic deformation in nanocrystalline grain interiors occurs by the emission of **complete dislocations** from grain boundaries, and below which the plastic deformation occurs by the emission of **partial dislocations**.

The slip systems in an fcc crystal with full dislocations when the grain size $d > d_c$, are the standard twelve $\{111\}\langle 110 \rangle$ systems. For full dislocations, slip can occur in either the positive or negative $\langle 110 \rangle$ -type direction on a $\{111\}$ -type plane. The twelve faulting systems for partial dislocations when $d \leq d_c$, are identical to the classical $\{111\}\langle 11\bar{2} \rangle$ twin systems for fcc materials [24]. Since the underlying atomic arrangement is polar in nature, we assume that faulting (like twinning) can occur in only one $\langle 11\bar{2} \rangle$ -type direction on a $\{111\}$ plane. We use the systems corresponding to the easy direction of faulting in our calculations. Note that we do not explicitly consider twinning as an explicit deformation mechanism in this paper.

For grain sizes $d > d_c$, the slip resistance s^{α} is given by

$$s^{\alpha} = Gb/d \quad (11)$$

and the corresponding microshear rate is given by

$$v^{\alpha} = v_0 \left(\frac{|\tau^{\alpha}|}{s^{\alpha}} \right)^{1/m} \text{sign}(\tau^{\alpha}). \quad (12)$$

For grain sizes $d \leq d_c$, the slip resistance s^{α} is given by¹

$$s^{\alpha} = Gb/(3d). \quad (13)$$

In this case there also exists a threshold resistance

$$s_{\text{th}} = \Gamma/b \quad (14)$$

and the corresponding microshear rate is given by

$$v^{\alpha} = \begin{cases} v_0 \left(\frac{\tau^{\alpha} - s_{\text{th}}}{s^{\alpha}} \right)^{1/m} & \text{if } (\tau^{\alpha} - s_{\text{th}}) > 0, \\ 0 & \text{otherwise.} \end{cases} \quad (15)$$

4. Simulation of an amorphous grain-boundary region

Before we proceed to the application of our plasticity theories to modeling the response of nanocrystalline materials, in this section we consider the deformation and failure response of a prototypical “grain-boundary” as modeled by our theory for amorphous materials. Fig. 1a shows a finite-element model of an amorphous grain-boundary region “GB” sandwiched between elastic layers “A”. The bottom edge of the sandwiched layer is held fixed, while \mathbf{u} denotes the displacement of the top edge. Several material parameters are required in the constitutive model to describe the mechanical behavior of an amorphous grain-boundary, cf. Section 2. These include the elastic shear moduli G and K , the cohesion c , the frictional coefficient μ , the viscoplasticity parameters v_0 and m ; the critical strains for cavitation failure $\epsilon_{c,\text{cr}}$ and $\epsilon_{c,\text{f}}$, and the parameters c_1 and c_2 controlling the evolution of cavitation resistance σ_{cr} . In this section we have chosen representative values to qualitatively demonstrate the mechanical response of a grain-boundary.² In order to model the *heterogeneity* of the grain boundaries, the initial value of the cohesion c for each grain-boundary element was randomly assigned a value from a list which had values of c uniformly distributed between 510 and 590 MPa. Fig. 1b shows a contour plot of the initial value of c in the grain-boundary region.

We first simulated the deformation of such an interface region to macroscopic simple shear, Fig. 2a. In this simulation we *suppressed* the cavitation mechanism. The nominal shear stress versus shear strain response of the grain-boundary region using representative values of material parameters for the amorphous layer is shown in Fig. 2b. A contour plot of the equivalent plastic strain, exhibiting inhomogeneous deformation involving “shear bands” in

¹ The factor of 3 difference between the resistances given in (11) and (13) arises because the energy per unit length of full dislocations is $(1/2)Gb_{\text{full}}^2$, while that of partial dislocations is $(1/2)Gb_{\text{partial}}^2$, and $b_{\text{partial}} = b_{\text{full}}/\sqrt{3}$.

² The precise magnitudes of the grain-boundary properties are not important here. They are discussed in greater detail in a later section where we apply our model to nc-Ni.

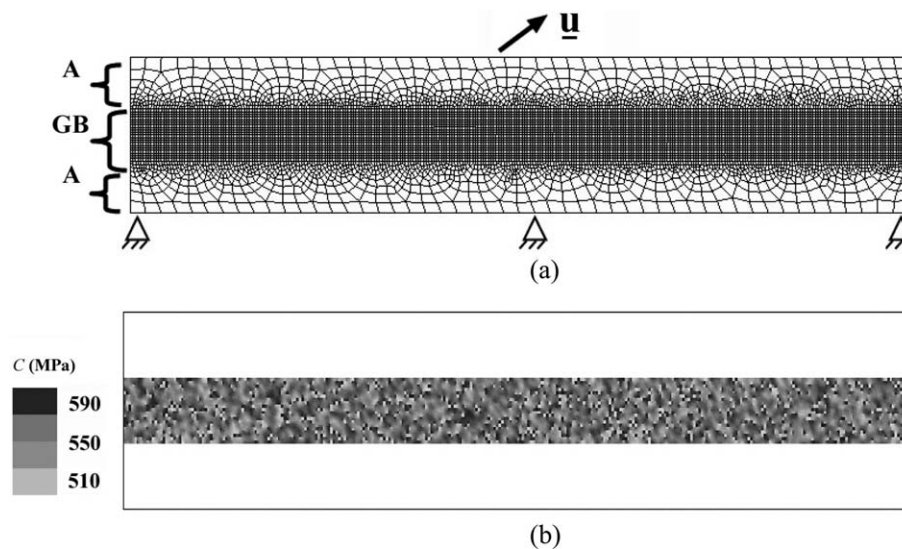


Fig. 1. (a) An amorphous grain-boundary region “GB” sandwiched between elastic layers “A”. The bottom edge of the sandwiched layer is held fixed, while \underline{u} denotes the displacement of the top edge. (b) A contour plot of the initial cohesion c assigned to the grain-boundary elements before deformation; the initial value of c for each grain-boundary element was randomly assigned a value from a list which had values of c uniformly distributed between 510 and 590 MPa.

the grain-boundary region after a nominal macroscopic shear strain of 50% is shown in Fig. 2c.

Next, cavitation failure in grain-boundary elements is also allowed. The top edge of the sandwich layer, cf. Fig. 1, was given displacements \underline{u}_{90} , \underline{u}_{45} , and \underline{u}_0 , respectively. Fig. 3a and b, respectively, shows the resulting normal traction versus normal strain, and tangential traction versus tangential shear strain curves from the three simulations. Fig. 3c shows the failure pattern corresponding to

the point “X” marked on the normal traction versus normal strain curve in Fig. 3a for the case \underline{u}_{90} . Cavities initiate in the grain-boundary region, grow and coalesce very quickly, and result in a progressive drop of the traction in the normal direction. Fig. 3d shows the failure pattern corresponding to the point “X” marked on the normal traction versus normal strain curve in Fig. 3a for the case \underline{u}_{45} . Finally, Fig. 3e shows the failure pattern corresponding to the point “a” marked on the tangential traction

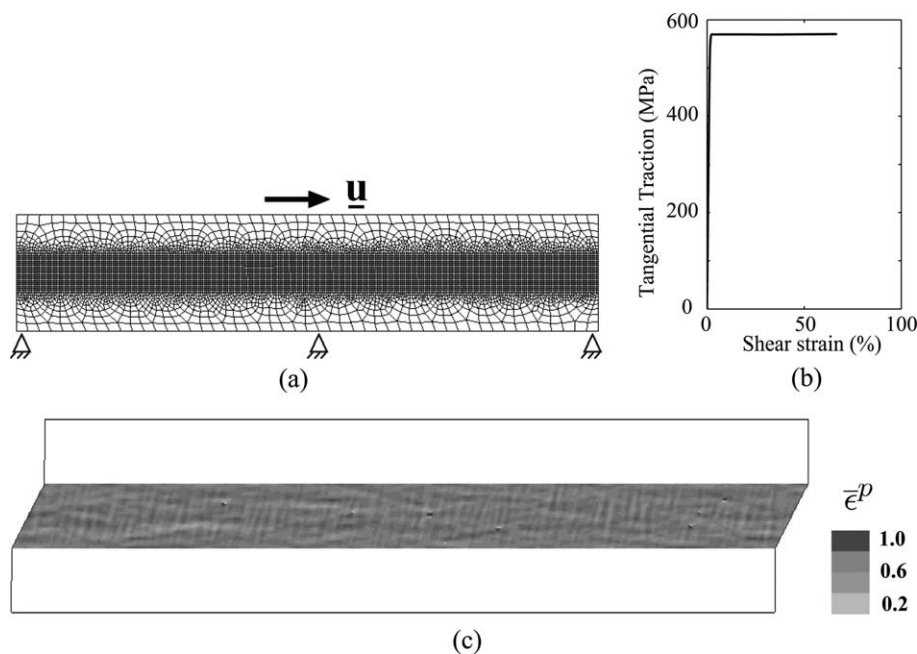


Fig. 2. (a) Shear response of an amorphous grain-boundary region. The bottom edge of the sandwiched layer is held fixed, while the top edge is displaced by \underline{u} to produce a simple shear deformation. (b) Nominal shear stress versus shear strain response of the grain-boundary region in simple shear, using representative values of material parameters for the amorphous layer. (c) A contour plot of the equivalent plastic strain, showing inhomogeneous deformation in grain-boundary region after a shear strain of 50%.

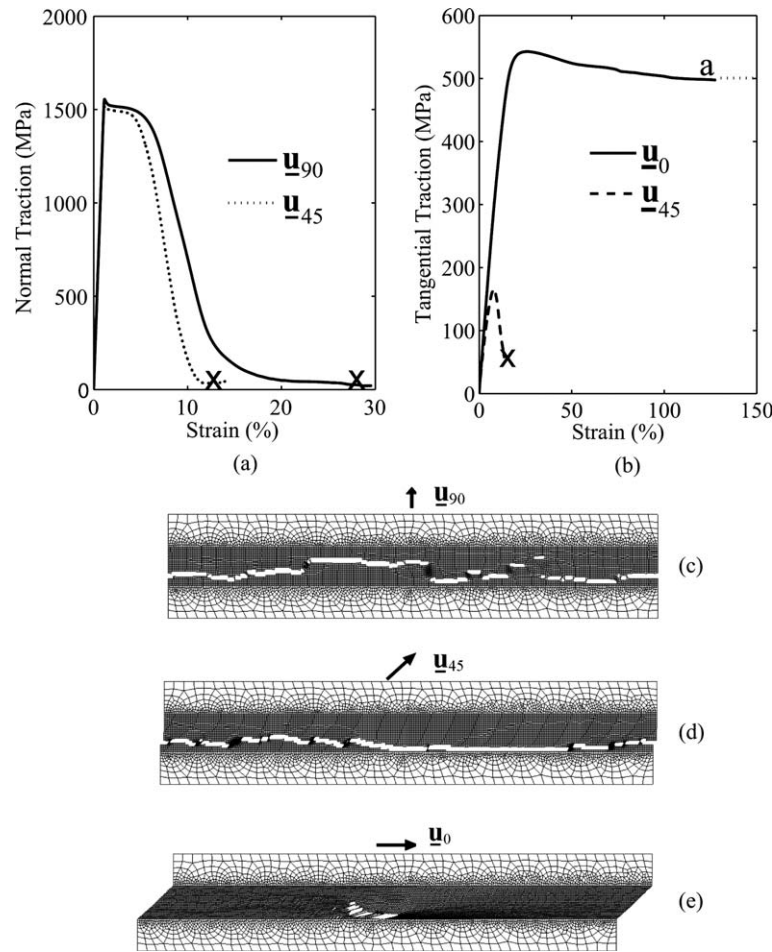


Fig. 3. (a) Normal traction versus nominal normal strain of the amorphous layer for \underline{u}_{90} and \underline{u}_{45} . (b) Tangential traction versus nominal shear strain of the amorphous layer for \underline{u}_0 and \underline{u}_{45} . (c) Failure pattern of the amorphous grain-boundary region subject to normal displacement \underline{u}_{90} . (d) Failure pattern for \underline{u}_{45} . (e) Failure pattern for \underline{u}_0 .

versus shear strain curve in Fig. 3b for the case \underline{u}_0 . The tangential traction versus shear strain curve shown in Fig. 3b indicates that even though there is some damage which initiates in the highly constrained regions, Fig. 3c, the shear strength of the grain-boundary decreases only slightly in simple shear.

In nanocrystalline materials, it is the interplay between the response of “amorphous” grain boundaries and crystalline grain interiors that dictates the overall deformation and failure behavior. In the following section, we discuss how to numerically generate representative microstructures which include different relative volume fractions of grain boundaries and grain interiors. These microstructures, coupled with appropriate constitutive models, will enable us to numerically study the competition between the deformation of grain interiors and grain-boundary regions in nanocrystalline materials with different grain sizes.

5. Finite-element representation of microstructures with different grain sizes

As shown schematically in Fig. 4a and b, for a fixed grain-boundary thickness of $2\delta = 1$ nm, the volume frac-

tion of grain-boundary regions decreases as the grain size d increases from 10 nm to 20 nm. Hence, by assuming that the physical thickness of a grain-boundary is fixed at ≈ 1 nm, we can numerically represent microstructures with different average grain size, by simply adjusting the volume

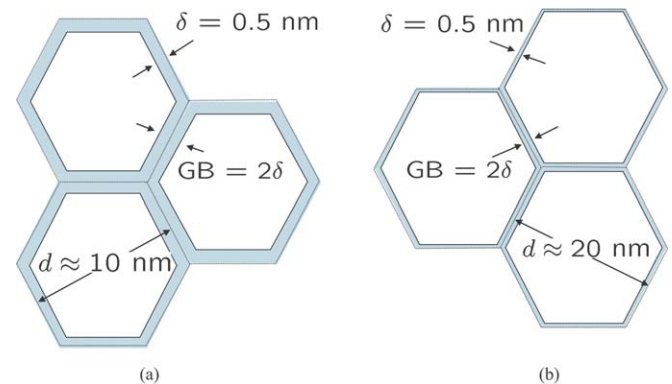


Fig. 4. Schematic of (a) grain size of $d = 10$ nm with grain-boundary regions of thickness $2\delta = 1$ nm; (b) grain size of $d = 20$ nm with grain-boundary region of thickness $2\delta = 1$ nm.

fraction of “grain-boundary” elements to “grain-interior” elements in a finite-element mesh.

Two-dimensional Voronoi-tessellated grains have been generated and meshed to represent the plane strain deformation of nanocrystalline metals. Fig. 5a–d shows four microstructures of average grain size of ≈ 10 nm, 20 nm, 34 nm, and 50 nm, respectively. The lighter-colored regions in these figures are the grain-boundary regions, and the darker regions are the grain interiors. In Fig. 5c the boxed

region is magnified to show the finite elements in the grain-boundary regions and the grain interiors. Note that unlike Fig. 1, here for computational efficiency *all grain-boundary regions are meshed with only one element through their thicknesses*. Thus, in order to obtain a high quality mesh for grain-boundary regions which are one element thick, the larger the grain size, the smaller the element size in the finite-element mesh that is required; this results in a large number of elements in the microstructure with larger grain

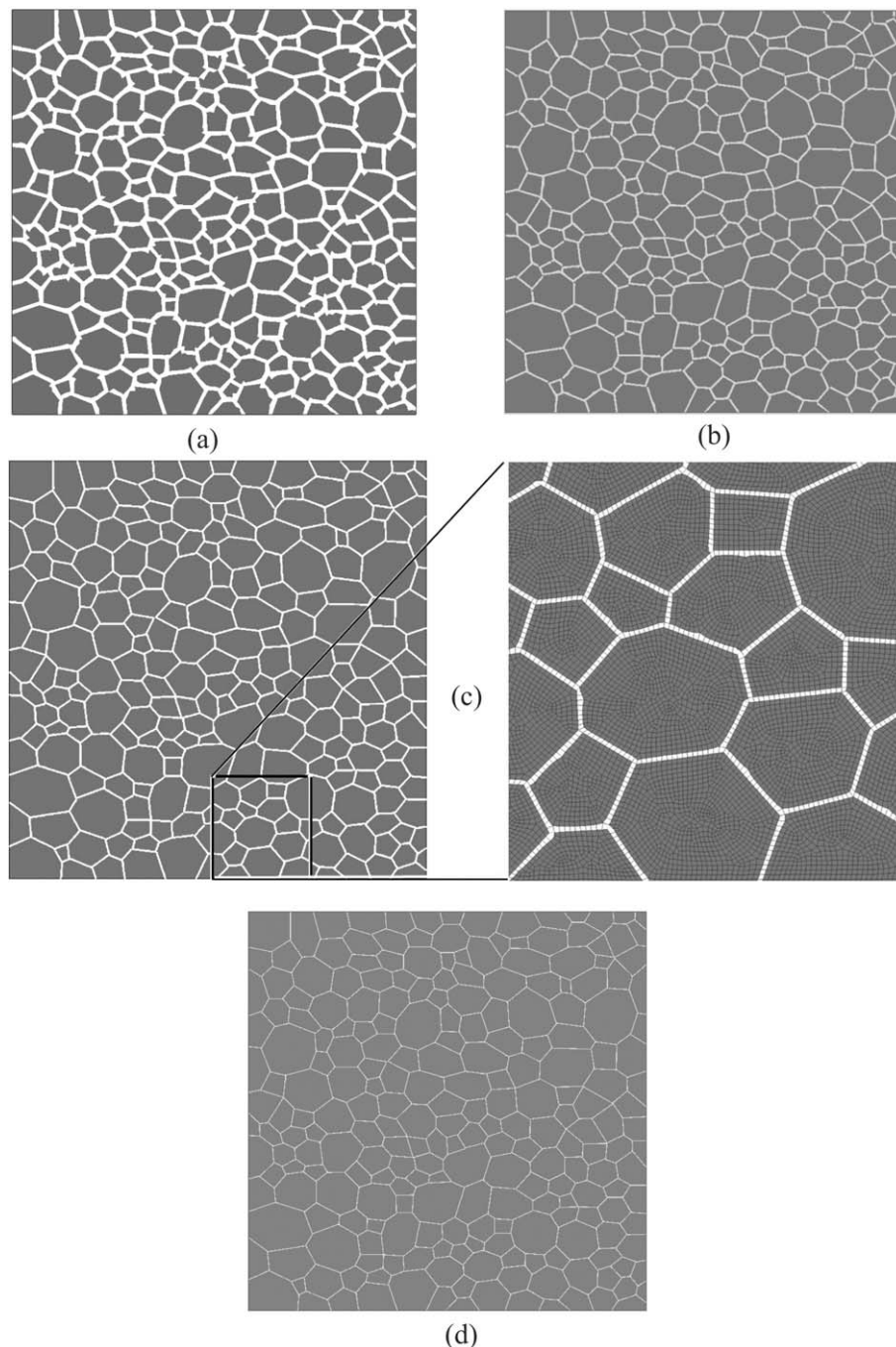


Fig. 5. Microstructures with an average grain size of (a) 10 nm; (b) 20 nm; (c) 34 nm; the boxed region is magnified to show finite-element meshes in grain interiors and grain boundaries; (d) 50 nm.

sizes. For example, in the microstructure shown in Fig. 5d, more than 300,000 elements were used to represent the microstructure for a grain size of $d \approx 50$ nm.

The constitutive response of the grain-boundary elements is represented by the model detailed in Section 2 for amorphous metals, while the constitutive response of the grain-interior elements is represented by the single-crystal plasticity model detailed in Section 3.

6. Application of the model to nanocrystalline nickel

The tensile stress–strain response of nanocrystalline nickel (nc-Ni) has been experimentally investigated by numerous groups (e.g. [10,16,25]). For example, Fig. 6 from [16] shows room temperature tensile stress–strain curves for nc-Ni with a grain size of ≈ 35 nm at three different strain-rates. The material exhibits a high strength of approximately 1500 MPa, but a low ductility of less than 5%. As noted earlier, it also exhibits a positive strain-rate sensitive response, with the rate sensitivity significantly higher than that observed in microcrystalline nickel at the same temperature.

In order to use our constitutive models for grain-interior crystal plasticity and grain-boundary amorphous plasticity to reproduce the macroscopic stress–strain curves for nc-Ni in Fig. 6, we need to estimate reasonable values for the material parameters appearing in these models. We discuss our estimation procedure in the sections below. Briefly, reasonable values for the grain-interior material properties are readily arrived at from physical considerations, but the properties of the grain boundaries need to be estimated by curve-fitting the macroscopic stress–strain curves. Our strategy is to estimate the material parameters by fitting the model to the stress–strain curves of [16] shown in Fig. 6, and then to check whether these values are reasonable or otherwise,

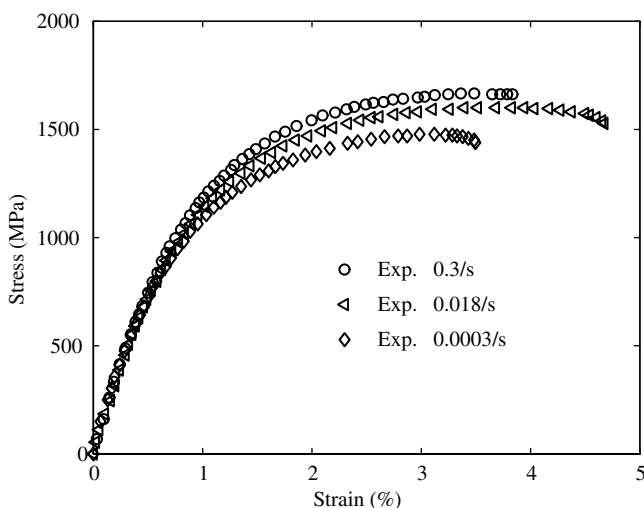


Fig. 6. Tensile stress–strain curves for nanocrystalline nickel with an average grain size of ≈ 35 nm at different quasi-static strain rates, Schwaiger et al. [16].

by checking whether the model with the material parameters so estimated, is able to reproduce a different set of data for a different grain size and different strain rates reported by Zhu et al. [10].

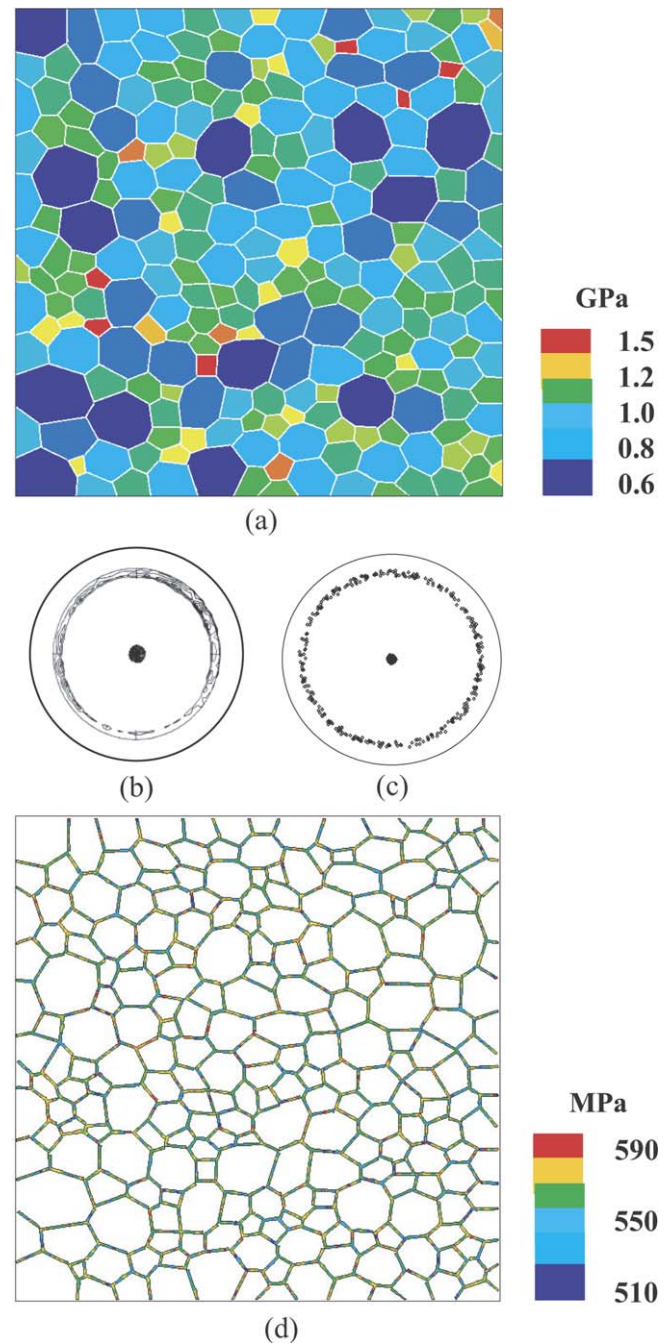


Fig. 7. (a) Grain-interior strength for the microstructure with an average grain size of ≈ 34 nm. (b) Experimental (111) pole figure of as-received electrodeposited nc-nickel sheet from Xiao et al. [27]; pole figure projection direction is normal to the plane of the sheet specimen. (c) (111) Pole figures corresponding to the grain orientations used in the polycrystal simulations. (d) Heterogeneity of grain-boundary cohesion. Cohesion in grain-boundary elements is randomly distributed in the range 510–590 MPa.

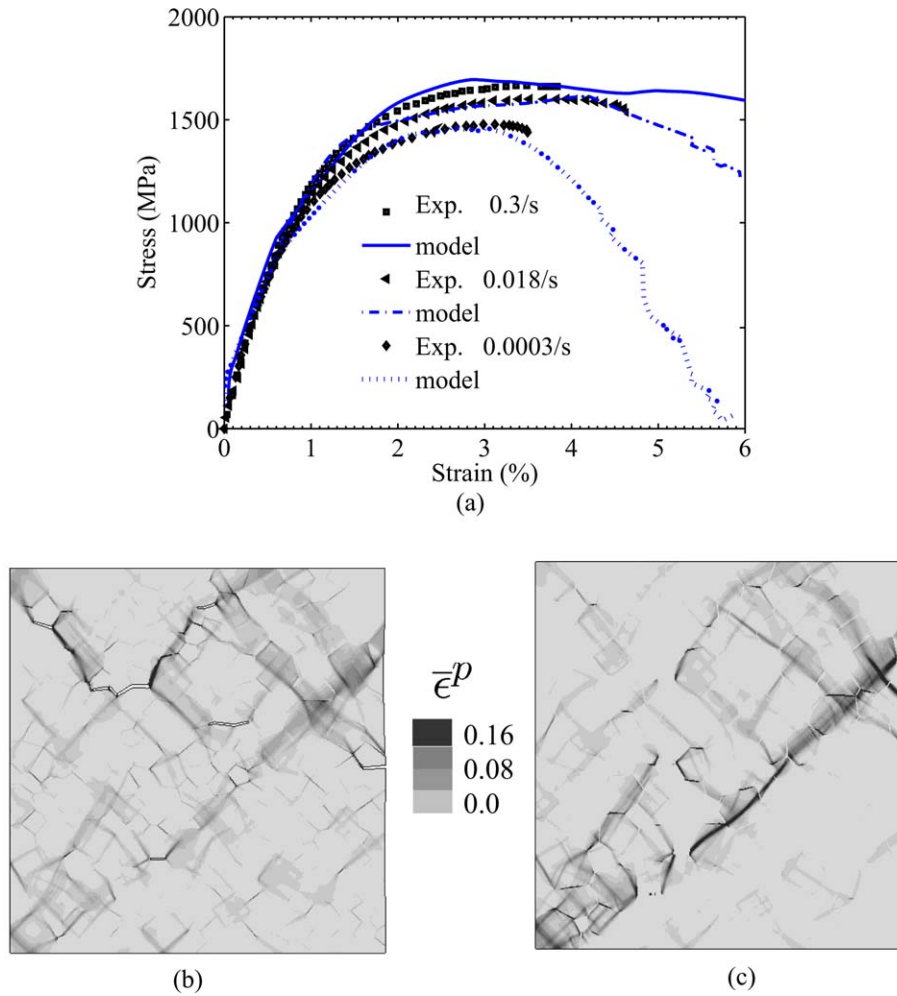


Fig. 8. (a) Comparison of numerically-calculated and experimentally-measured [16] stress–strain curves. Equivalent plastic strain contour after 5% strain; (b) at a strain rate of $\dot{\epsilon} = 3 \times 10^{-4}$ /s; voids in the figure result from grain-boundary elements which have failed due to cavitation; (c) at a strain rate of $\dot{\epsilon} = 3 \times 10^{-1}$ /s. At this higher strain rate, the high rate-sensitivity of the grain-boundary elements results in stronger grain boundaries, and this induces dramatically-increased grain-interior plasticity.

6.1. Material properties for grain interiors

The values of the anisotropic elastic constants for nickel are taken as, $C_{11} = 247$ GPa, $C_{12} = 147$ GPa, $C_{44} = 125$ GPa [26]. Next, with $G \approx 79$ GPa, a nominal shear modulus, $b = 0.249$ nm the magnitude of the Burgers' vector, and $\Gamma \approx Gb/100$ the surface energy, the critical grain size below which partial dislocations emitted from grain boundaries are the dominant carriers of plastic deformation of the grain interiors is given by $d_c \approx (2/3)(Gb^2/\Gamma) \approx 16.6$ nm. The slip systems for $d > d_c$, and the faulting systems for $d \leq d_c$ are $\{111\}\langle 110 \rangle$ and $\{111\}\langle 11\bar{2} \rangle$, respectively, and the slip and faulting system resistances are taken as $s^z = Gb/d$ for $d > d_c$, and $s^z = Gb/3d$ for $d \leq d_c$. If for the very smallest grain sizes the resistance calculated using this estimate exceeds the ideal shear strength $s_{\max}^z \approx G/30 \approx 2.6$ GPa, then the resistance is capped at this maximum possible value. Fig. 7a shows a contour plot of the grain-interior strength for a microstructure with an average grain-size of 34 nm.

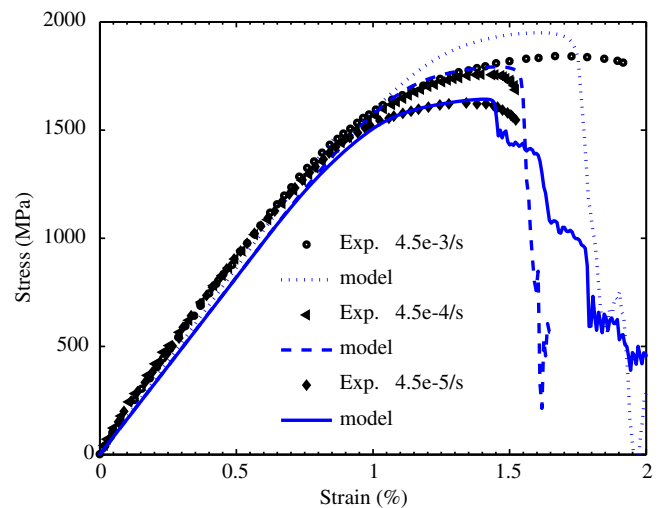


Fig. 9. Comparison of predicted stress–strain curves at different strain-rates for nc-Ni with an average grain size of 20 nm against corresponding experimental data from Zhu et al. [10].

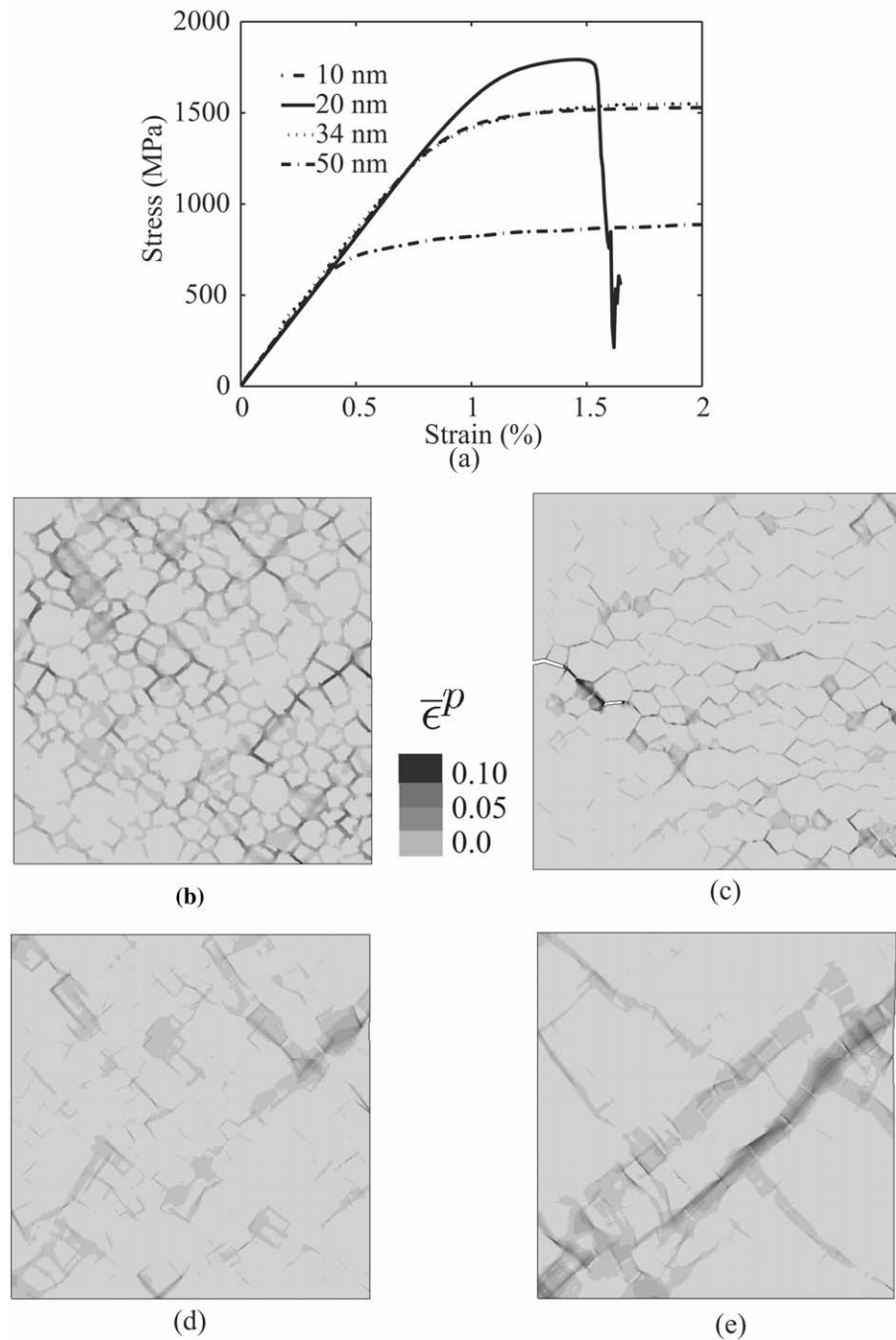


Fig. 10. (a) Tensile stress–strain curves for different grain sizes at a strain rate of 3×10^{-4} /s. Corresponding contours of plastic strain at a macroscopic strain of 1.5%: (b) 10 nm; (c) 20 nm; (d) 34 nm; and (e) 50 nm.

Nanocrystalline nickel produced by electrodeposition typically possesses a strong crystallographic texture. Fig. 7b shows a (111) pole figure for such a material; the pole figure projection direction is normal to the plane of the sheet nc-Ni specimen. In our numerical simulations the lattices of the individual grains were assigned a set of orientations that approximate this initial texture, Fig. 7c. Fig. 5 shows self-similar microstructures with different average grain sizes. For each of these different average

grain-sized microstructures, the initial lattice orientation of each grain is taken to be the same for the four different microstructures; hence the resulting overall crystallographic texture for all the different microstructures of Fig. 5 is as shown in Fig. 7c.

The reference strain rate v_0 and strain-rate sensitivity parameter m in (12) and (15) are taken as $v_0 = 10^{-5}$ /s, and $m = 0.005$; the low value of the parameter m is meant to represent an approximately rate-independent response

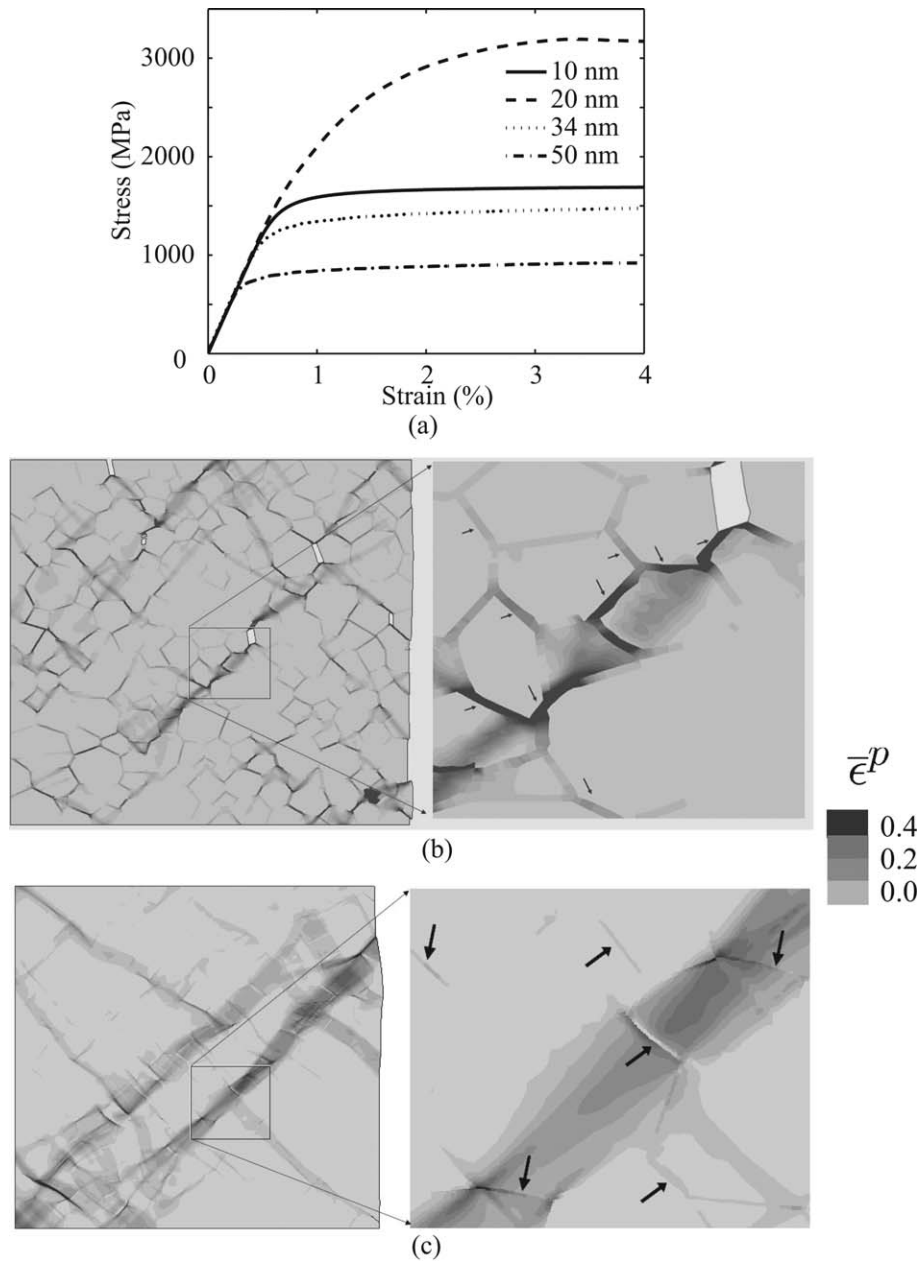


Fig. 11. (a) Compression stress–strain curves for different grain sizes at a strain rate of 3×10^{-4} /s. Corresponding contours of plastic strain at a macroscopic strain of 4%: (b) 20 nm and (c) 50 nm. In (b) and (c) a small region of the microstructure is magnified to show the severe deformation of grain-boundary regions marked by arrows.

for the plasticity of the grain-interiors. The threshold resistance s_{th} for partial dislocation emission in (15) is taken as $s_{th} = \Gamma/b \approx 790$ GPa.

6.2. Material properties for grain boundaries

Having arrived at physically plausible values for the grain-interior material properties, we next estimate the properties of the grain boundaries by curve-fitting the macroscopic stress–strain curves of [16] shown in Fig. 6. Since the average grain size in the material tested by [16] is ≈ 30 – 40 nm. We have used the microstructure with average

grain size of 34 nm, Fig. 5c, to estimate the grain-boundary properties.

The elastic properties of grain-boundaries are assumed to be the same as those for polycrystalline nickel with $G = 79$ GPa and $K = 182$ GPa. To allow for varying grain-boundary strengths, the value of the c for each grain-boundary element was randomly assigned a value from a list which had values of c uniformly distributed between 510 and 590 MPa, so that the average value of the cohesion of the grain boundaries is $c_{av} = 550$ MPa. Fig. 7d shows a contour plot of the values of the initial cohesion in the grain boundaries. We use a small value of

frictional coefficient $\mu = 0.04$, which is close to the internal frictional coefficient of metallic glass [19].³ The reference strain rate and strain-rate sensitivity parameter in (5) and (6) are taken as $v_0 = 10^{-5}/\text{s}$, and $m = 0.1$, while the parameters governing the cavitation resistance in (6) are taken as $c_1 = 10 \text{ GPa}$, and $c_2 = 8.5$ and the parameters appearing in the definition of cavitation damage (8), are taken as $\epsilon_{\text{cr}}^p = 0.10$, and $\epsilon_f^p = 0.36$, respectively.

Using our previously-listed assumptions concerning the grain-interior properties and the inelastic parameters for the grain boundaries listed above, we obtained the reasonable curve-fit shown in Fig. 8a, to the experimentally-measured stress–strain curves [16].⁴

Fig. 8b shows a contour plot of the equivalent plastic strain after 5% strain at a strain rate of $\dot{\epsilon} = 3 \times 10^{-4}/\text{s}$. At this low strain rate most of the inelastic deformation is restricted to the grain-boundary elements, and due to the constrained deformation in these boundaries, cavitation occurs. The voids observed in Fig. 8b result from grain-boundary elements which have failed due to cavitation. In contrast, Fig. 8c shows a contour plot of the equivalent plastic strain after 5% strain at a strain rate of $\dot{\epsilon} = 3 \times 10^{-1}/\text{s}$. At this higher strain rate the high rate-sensitivity of the grain-boundary elements results in stronger grain boundaries, and this induces dramatically increased grain-interior plasticity, as evidenced by the plastic strain contours in this figure. Also, comparing Fig. 8c to Fig. 8b, we note that the amount of cavitation damage at the grain boundaries is substantially reduced at the higher strain rate.

Next, in order to check whether the material parameters estimated for the grain interiors and grain boundaries are in a reasonable range, we verified the predictive capability of the model by comparing the predicted stress–strain curves at different strain-rates for nc-Ni with an average grain size of 20 nm using the mesh shown in Fig. 5b against corresponding experimental data from [10]. The comparison, Fig. 9, shows that while stress levels are reasonably well-predicted, the ductility is not well-predicted by our relatively crude grain-boundary cavitation damage model.

6.3. Effect of grain size variation on the stress–strain response in tension

With the material parameters for the grain interior and grain boundaries fixed at values determined in the previous subsections, Fig. 10a shows tensile stress–strain curves for different grain-sized microstructures of Fig. 5, at a strain rate of $3 \times 10^{-4}/\text{s}$. As is clear, the peak strength does not increase monotonically as the grain size is reduced.

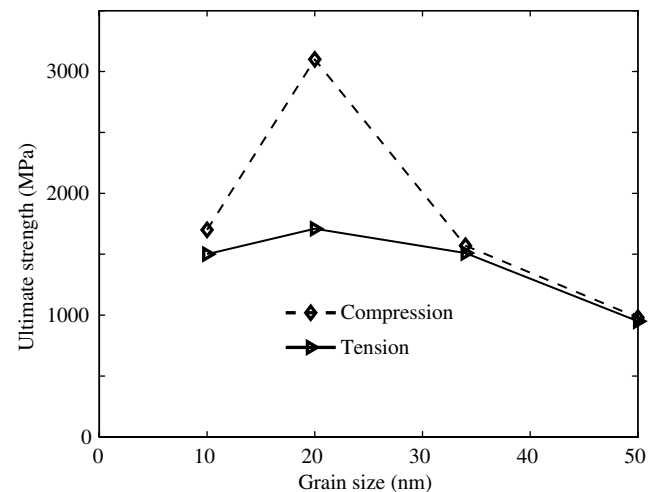


Fig. 12. Comparison of ultimate strength in tension and compression versus grain size.

Although we have results for only four different grain sizes, a clear peak is observed for the microstructure with a grain size of 20 nm; the peak strengths for the 10 nm and 34 nm microstructures are clearly lower than that for the 20 nm microstructure. Fig. 10b–d shows contour plots of the equivalent plastic strain at the peak strength levels for the different grain sizes. As is clear from these figures, at the smaller grain sizes of 10, 20 and 34 nm most of the inelastic deformation occurs at the grain boundaries, while the larger 50 nm grain-sized microstructure shows substantial grain-interior plasticity.

6.4. Effect of grain size variation on the stress–strain response in compression

In this section we numerically investigate the response of nc-Ni in compression.⁵ Fig. 11a shows tensile stress–strain curves for different grain-sized microstructures of Fig. 5, at a strain rate of $3 \times 10^{-4}/\text{s}$. Fig. 11b and c shows contour plots of the equivalent plastic strain at a macroscopic strain of 4% for microstructures of 20 nm and 50 nm average grain-sizes, respectively. For clarity, in each of Fig. 11b and c, a small region of the deformed microstructure is magnified to show the severe deformation of grain-boundary regions marked by arrows. The smaller grain-sized microstructure of Fig. 11b shows substantial grain-boundary shearing and cavitation, with some grain-interior plasticity in the grains associated with boundaries with intense shearing activity. As the grain size increases to 50 nm, Fig. 11c shows a transition to increased grain-interior plasticity and inhomogeneous deformation patterns resembling “shear-bands” which traverse several grains.

A plot of ultimate strength in tension and compression versus grain size is shown in Fig. 12. There is a clear

³ The precise value of μ is not consequential here.

⁴ The value of strain-rate sensitivity of $m = 0.1$ appears high, but this is the value that gives us the fit to the macroscopic stress–strain curves shown in Fig. 8a. We emphasize that we do not mean to imply that in the fully-amorphous limit the material would exhibit such a high strain-rate sensitivity.

⁵ We were unable to find experimental data for controlled compression tests on nc-Ni in the literature.

strength-differential effect, with compressive strengths being higher than tensile strengths for the 10 nm, 20 nm, and 34 nm grain-sized microstructures. Our calculations show that this strength-differential effect is *not primarily due* to the small friction coefficient of $\mu = 0.04$ for the grain-boundary model, but arises because of the delayed damage by cavitation of grain boundaries in compression, relative to the situation for tension.

7. Concluding remarks

We have developed a finite-element-based two-dimensional plane-strain mesoscale model to numerically study the deformation and failure behavior of nanocrystalline fcc metals. A rate-dependent amorphous plasticity model which accounts for cavitation and related failure phenomena is used to model the grain-boundary, while a crystal-plasticity model which accounts for the transition from partial dislocation to complete dislocation mediated plasticity is used for the limited plasticity of the grain interiors. Numerical simulations using material parameters estimated to represent the macroscopic rate-dependent stress–strain response of nc-Ni show that:

- There is a deformation mechanism transition from grain-interior dominated shearing to grain-boundary dominated shearing and cavitation as the average grain-size decreases from 50 nm to 10 nm.
- A change from low strain rate to high strain rate deformation also induces a transition in mechanism from deformation dominated by grain-boundary shearing and cavitation to grain-interior dominated plastic deformation.
- The low ductility in nc-Ni is the result of intergranular failure due to grain-boundary shearing and resulting cavitation at triple-junctions and other high stress points in the microstructure.
- The strength of nc-Ni is expected to be higher in compression than in tension, primarily due to the easier operation of cavitation failure of the grain boundaries in tension relative to that in compression.

Acknowledgements

Discussions with Professors Subra Suresh, Sharvan Kumar, and Chris Schuh are gratefully acknowledged. Financial support was provided by the ONR Contract N00014-01-1-0808 with MIT.

References

- [1] Gleiter H. Acta Mater 2000;48:1.
- [2] Weertman JR. In: Koch C, editor. Nanostructured materials. NY: Noyes; 2002. p. 393.
- [3] Kumar KS, Van Swygenhoven H, Suresh S. Acta Mater 2003;51:5743.
- [4] Wolf D, Yamakov V, Phillpot SR, Mukherjee A, Gleiter H. Acta Mater 2005;53:1.
- [5] Ranganathan S, Divakar R, Ragunathan VS. Scripta Mater 2001;44:1169.
- [6] Farkas D, Van Swygenhoven H, Derlet PM. Phys Rev B 2002;66:60101.
- [7] Sansoz F, Molinari JF. Scripta Mater 2004;50:1283.
- [8] Farkas D, Petegem SV, Derlet PM, Van Swygenhoven H. Acta Mater 2005;53:3115.
- [9] Asaro RJ, Krysl P, Kad B. Phil Mag Lett 2003;83:733.
- [10] Zhu B, Asaro RJ, Krysl P, Bailey R. Acta Mater 2005;53:4825.
- [11] Van Vliet KJ, Tsikata S, Suresh S. Appl Phys Lett 2003;83:1441.
- [12] Yip S. Nature Mater 2004;3:11.
- [13] Yamakov V, Wolf D, Phillpot SR, Mukherjee AK, Gleiter H. Nature Mater 2004;3:43.
- [14] Deng D, Argon AS, Yip S. Philos Trans Roy Soc A 1989;329:613.
- [15] Anand L, Kalidindi SR. Mech Mater 1994;17:223.
- [16] Schwaiger R, Moser B, Dao M, Chollacoop N, Suresh S. Acta Mater 2003;51:5159.
- [17] Wei YJ, Anand L. J Mech Phys Solids 2004;52:2587.
- [18] Warner DH, Sansoz F, Molinari JF. Int J Plasticity 2006;22:754.
- [19] Anand L, Su C. J Mech Phys Solids 2005;53:1362.
- [20] Su C, Anand L. Acta Mater 2006;54:179.
- [21] Asaro RJ, Needleman A. Acta Metall 1985;33:923.
- [22] Kalidindi SR, Bronkhorst CA, Anand L. J Mech Phys Solids 1992;40:537.
- [23] Asaro RJ, Suresh S. Acta Mater 2005;53:3369.
- [24] Staroselsky A, Anand L. J Mech Phys Solids 1998;46:671.
- [25] Torre FD, Van Swygenhoven H, Victoria M. Acta Mater 2002;50:3957.
- [26] Simmons G, Wang H. Single crystal elastic constants and calculated aggregate properties. Cambridge, MA: MIT Press; 1971.
- [27] Xiao CH, Mirshams RA, Whang SH, Yin WM. Mater Sci Eng A 2001;301:35.